Improving discrete element simulations of sea ice break up: Applications to Nares Strait

Brendan West[1], Devin O'Connor[1], Matthew Parno[1,2], Max Krackow[1], Chris Polashenski[1,3]

[1]Cold Regions Research and Engineering Laboratory, U.S. Army Corps of Engineers, Hanover, NH, USA
[2]Department of Mathematics, Dartmouth College, Hanover, NH, USA
[3]Thayer School of Engineering, Dartmouth College, Hanover, NH, USA

Key Points:

- The DEM with bonded particles and physics-based fracture models can accurately capture the behavior of sea ice over varying spatial scales.
- Fracture is captured with a non-local stress calculation and Mohr-Coulumb failure model to determine when inter-particle bonds fail.
- The shape and extent of the DEM ice particles are initialized from remote sensing observations of ice.

Corresponding author: B. West, `brendan.a.west@erdc.dren.mil`

Abstract

Particle methods can provide detailed descriptions of sea ice dynamics that explicitly model fracture and discontinuities in the ice, which are difficult to capture with traditional continuum approaches. We use the ParticLS software library to develop a discrete element method (DEM) model for sea ice dynamics at regional scales and smaller (<100 km). We model the sea ice as a collection of discrete rigid particles that are initially bonded together using a cohesive beam model that approximates the response of an Euler-Bernoulli beam located between particle centroids. Ice fracture and lead formation are determined based on the value of a non-local stress state around each particle and a Mohr-Coulomb fracture model. Therefore, large ice floes are modeled as continuous objects made up of many bonded particles that can interact with each other, deform, and fracture. We generate realistic particle configurations by discretizing the ice in MODIS satellite imagery into polygonal floes that fill the ice shape and extent that occurred in nature. The model is tested on ice advecting through an idealized channel and through Nares Strait. The results indicate that the bonded DEM model is capable of capturing the behavior of sea ice over a wide range of spatial scales, as well as the dynamic sea ice patterns through constrictions (arching, lead formation).

Plain Language Summary

Models of sea ice give researchers important tools to study how the Arctic is changing. At very large scales ($>$ 100 km) most models treat the ice as a continuous material. However, sea ice is naturally broken into many pieces. The geometry of these pieces impacts mechanical behavior, and as a result the conventional modeling approaches break down at smaller scales. Discrete element method (DEM) models instead treat ice as a collection of individual rigid bodies that can interact with each other independently, and therefore can capture the discontinuities and geometric force concentrations in ice that are common at small scales. In this paper, we extend DEM approaches to model behavior of sea ice across a wide range of spatial scales in a single modeling framework. We adapt a new method for evaluating the stress state within the modeled ice (bonded DEM particles) to determine when the ice should fracture. As a result, the model simulates large pieces of ice that can break into smaller pieces, or floes, composed of many still-bonded particles. This allows us to represent both discrete fractures, and emergent aggregate behavior of ice as it deforms. As an example, we simulate ice advecting through Nares Strait.

1 Introduction

Numerical models of sea ice play an important role in understanding the changing Arctic and allow researchers to predict the dynamic response of sea ice to different environmental conditions. One of the most challenging aspects of modeling sea ice dynamics is capturing the behavior across a wide range of spatial scales. Sea ice deformation is well approximated by continuous behavior at large scales (>∼100 km), but at smaller scales (<∼10 km) the dynamics become highly-discontinuous resulting from interactions between many individual floes (Hunke et al., 2020) and discrete fracture events. Developing models that can simulate ice dynamics at smaller scales where continuum approaches break down, but which also produce realistic emergent continuum behavior is necessary to support a variety of stakeholder needs. For example, such scale-spanning simulations of fracture are needed for studying the Arctic energy balance. Lead size, prevalence, and persistence strongly influence solar energy budgets. Further, emergent dynamics impact advective ice balance, governing the advection of ice out of the Arctic Ocean. In addition, high resolution forecasts from predictive models are becoming increasingly important due to increased human activity in the Arctic. The recent decline in Arctic sea ice has lead to increased traffic in the Arctic Ocean for fishing, resource extraction, tourism, cargo shipping, and military purposes. This increase necessitates accurate forecasts of ice dynamics to provide these operations with critical information on where and when their vessels can safely travel through an ice-infested region. Models that can explicitly capture small discontinuities in the ice are particularly valuable for navigation.

Many sea ice models, such as those used in global climate models, employ continuum approaches where the sea ice is discretized with an Eulerian mesh and the ice is modeled with constitutive models such as viscous-plastic (VP) or elastic-viscous-plastic (EVP) rheologies (Hibler III, 1979), (Hunke & Dukowicz, 1997), (Hunke et al., 2020). These models are well-suited for simulating ice motion over large regions and long timescales, and have been shown to accurately capture important properties of the ice behavior (Hunke et al., 2020). However, their underlying continuum assumption begins to break down at smaller length scales where the ice is highly discontinuous (Rasmussen et al., 2010), (Damsgaard et al., 2018).

Several efforts have used the discrete element method (DEM) to simulate sea ice dynamics as an alternative to continuum approaches (Hopkins, 2004), (Hopkins & Thorndike, 2006), (Herman, 2013), (Herman, 2016), (Kulchitsky et al., 2017), (Damsgaard et al., 2018). The DEM explicitly models the dynamics of individual rigid bodies, or "particles", and can therefore capture discontinuities in sea ice such as cracks and leads that are common near the ice edge or in the marginal-ice-zone (MIZ), but cannot be adequately captured with traditional continuum methods. The DEM is a promising modeling approach for sea ice (Hunke et al., 2020), however many DEM sea ice studies to date have used simplified physics and particle geometries in order to lessen the computationally-intensive process of tracking and calculating the interaction between many particles. For example, it is common to use elastic, viscous-elastic, or Hertzian contact models to calculate inter-particle forces that do not account for the energy lost due to ridging between ice floes. It is also common to represent particles with disks or simple shapes due to the ease of solving contact between basic shapes (Sun & Shen, 2012), (Herman, 2013), (Herman, 2016), (Damsgaard et al., 2018), (Jou et al., 2019). Although these modifications increase the speed of the models, oversimplifying the complex geometries and interactions found in real sea ice is likely to limit the realism of these models.

In this paper we build upon recent DEM advances to present and evaluate a 2D framework that uses cohesively-bonded polygonal-shaped particles, and a non-local physics-based fracture model to capture the behavior of sea ice over varying spatial scales. We use a new DEM software library called ParticLS (Davis et al., 2021) that can represent sea ice floes with convex polygons to better capture the irregular shapes often observed in real sea ice. ParticLS implements the cohesive beam model (André et al., 2012), which was developed to simulate continuous materials as collections of bonded DEM particles. This cohesive model approximates the response of Euler-Bernoulli beams placed between centroids of adjacent particles to propagate stresses and strains through the bonded particle collection. These beams can break, thereby simulating discontinuities in the material.

Many DEM sea ice models have simulated cohesion between particles, however they have typically evaluated the local stress state within each bond to determine if they should break. (Damsgaard et al., 2018) and (Herman, 2016) compared the maximum normal and maximum shear stresses within the bonds against prescribed thresholds, while (Kulchitsky et al., 2017) compared the bond stresses against a Mohr-Coulomb failure envelope. Alternatively, (Hopkins, 2004) decreased the bond stress after a compressive or tensile threshold was reached, thereby gradually weakening the ice post-failure. We also employ a Mohr-Coulomb failure model due to its well-known ability to describe sea ice fracture, but we extend the approach by evaluating the non-local stress states of each particle to determine whether bonds should fail (André et al., 2013). This non-local stress approach considers the stress-state produced by all DEM particles within a small neighborhood, which has been shown to reproduce more accurate crack patterns in elastic brittle materials than localized bond fracture models (André et al., 2013), (André et al., 2017). We are unaware of applications of either the cohesive beam law or non-local stress evaluations in regional-scale DEM models of sea ice, or evaluations of their ability to capture salient sea ice behavior.

To test our model, we follow the precedent set by (Dumont et al., 2009), (Rasmussen et al., 2010), (Dansereau et al., 2017), and (Damsgaard et al., 2018), and simulate sea ice advecting through channel domains that encourage arch formation and failure. Ice arches are examples of large-scale sea ice behavior that result from small-scale interactions of ice parcels that jam in constricted regions. The arches form as distinct cracks across the constriction that completely stop and separate the ice upstream from the ice flowing downstream. These arches often result in long-lasting discontinuities in the ice. We use an idealized channel case from (Dansereau et al., 2017) to develop an understanding of the arching and break up process in a DEM setting, and then apply that knowledge to a more realistic simulation of the ice through Nares Strait (Figure 1). The Nares Strait arches are well-studied features that break up almost every spring, resulting in highly-discontinuous sea ice that advects out of the strait. We feel this offers a good test case for the DEM approach and its ability to simulate the emergent behavior arising from complex interaction between many deformable bodies of ice. These simulations also allow us to compare our model with continuum sea ice modeling approaches that have been used to simulate ice advecting through similar geometries (Dumont et al., 2009; Rasmussen et al., 2010; Dansereau et al., 2017; Damsgaard et al., 2018). These comparisons help us determine how well the DEM models the nature of sea ice deformation compared to other methods in the literature. Our results indicate the importance of non-local fracture criteria and demonstrate the broad utility of hybrid continuum-discrete DEM methods for capturing complex ice behavior.

Nares Strait is one of the most significant passageways for sea ice and freshwater to transport out of the Arctic Ocean and into the Atlantic, and the arching process plays an important role in limiting the amount of sea ice flux through the strait. Between 1997-2009, an average of $42.0 \times 10^3\,\mathrm{km}^2$ of sea ice left the Arctic Ocean through Nares Strait each year (Kwok et al., 2010). In 2007, a stable arch did not form and approximately $87.0 \times 10^3\,\mathrm{km}^2$ of sea ice advected through the strait, more than double the annual average, illustrating how important the formation and stability of these arches are to the Arctic sea ice balance (Kwok et al., 2010). The ice located north of Nares Strait is some of the oldest and thickest ice in the Arctic,

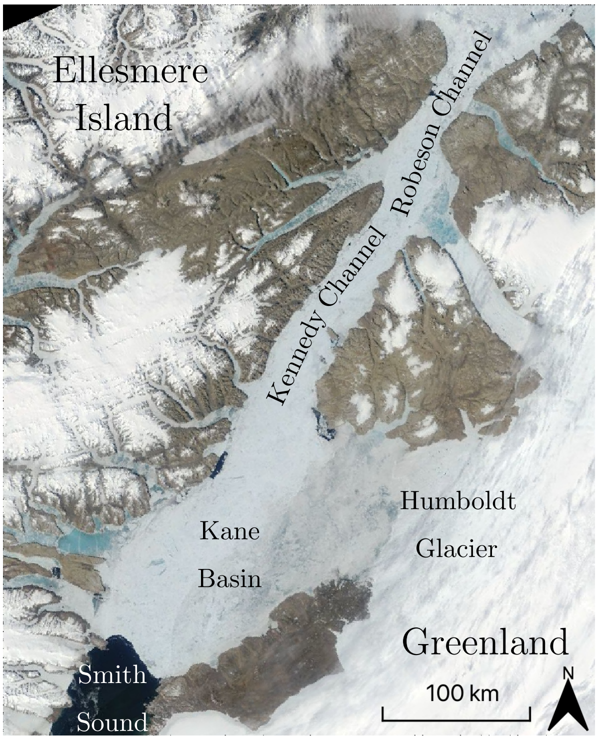

Figure 1: Map of Nares Strait region and sub-regions. The underlying MODIS image is from June 28, 2003, and reflects the ice extent and arch from which we initialized the floe DEM collection.

and the thinning of Arctic ice in recent years has led to a trend toward earlier arch failure in spring (Moore et al., 2021). The stability of the ice arches in Nares Strait therefore play an important role in preserving thick multi-year ice in the Lincoln Sea (Moore et al., 2021). Models, like the one proposed here, can capture arching behavior and can thus shed light on the mechanisms driving arch failure and ice advection through Nares Strait.

In the following sections we describe the governing equations, contact laws, and forcing functions that comprise our model. Section 2 describes the momentum balance driving the ice dynamics, and section 3 describes the DEM approach and different models used to simulate these resultant dynamics. In section 4 we describe the method used to initialize the particles from MODIS imagery. Sections 5 and 6 present the results of the idealized channel and Nares Strait simulations, and compares the Nares Strait results with behavior seen in optical satellite imagery. Section 7 discusses the effectiveness of this method in capturing the sea ice dynamics as well as potential improvements.

2 Momentum Balance on Sea Ice

The principal forces acting on sea ice include drag from wind and ocean currents (F_a and F_o), internal stress gradients within the ice (F_s), Coriolis forces (F_c), and forces due to sea surface tilt (F_t) (Hibler III, 1979), (Steele et al., 1997):

$$M_i \dot{u}_i(t) = F_a(x_i, t) + F_o(x_i, t) + F_s(x_i, t) + F_c(x_i, t) + F_t(x_i, t) \tag{1}$$

where M_i is the ice mass and $\dot{u}_i(t)$ is the ice acceleration. This force balance generally consists of wind driven forces trying to move the ice, with ocean drag and the internal ice stress resisting the motion (Thorndike & Colony, 1982). As a result, the motion of ice in free drift is typically dominated by wind and ocean currents, whereas the internal ice stress dominates when the ice is consolidated or constricted (Steele et al., 1997). The Coriolis and surface tilt terms are usually small (Steele et al., 1997), especially for ice dynamics over the span of a few days and over smaller spatial scales (Wadhams, 2000). In addition, (Rallabandi et al., 2017) notes that the Coriolis force is diminished within narrow straits because the force typically acts normal to the direction of flow. We assume a stagnant ocean current, which means the force due to a gradient in surface height is zero (Dansereau et al., 2016). Therefore, we ignore the affects of Coriolis and surface tilt forces acting on the ice in our simulations. The DEM also accounts for the forces generated between neighboring particles, and therefore includes an external force due to contacts ($F_e(x_i, t)$). The final momentum balance in the DEM simulations is therefore:

$$M \dot{u}_i(t) = F_a(x_i, t) + F_o(x_i, t) + F_s(x_i, t) + F_e(x_i, t) \tag{2}$$

In subsequent sections we describe the cohesion model used to capture the internal stress state within consolidated ice, the contact models describing the forces generated between particles, and the drag force model used to account for wind and ocean currents.

3 DEM Model Overview

The DEM was first applied to sea ice in the 1990's (Hopkins & Hibler, 1991), (Løset, 1994b), (Løset, 1994a), (Jirásek & Bažant, 1995), (Hopkins, 1996), and it was shown as an effective method for modeling the interactions between individual ice floes. The DEM calculates the forces and torques acting on a particle at each time step, and then updates its motion and orientation through numerical integration:

$$m_i \dot{u}_i(t) = \sum_{j=1}^{n} f_{i,j}(t) + f_{i,s}(t) \tag{3}$$

where (subscripts i and j indicate quantities corresponding to a home particle i and neighboring particle j, respectively)

- m_i is the mass of the i-th particle,
- $\dot{u}_i(t)$ is the particle's acceleration,
- $f_{i,j}(t)$ is the force acting on particle i from particle j,
- $f_{i,s}(t)$ are forces acting on the surfaces of the particle,

$$I_i \dot{\omega}_i(t) = \sum_{j=1}^{n} \tau_{i,j}(t) + \tau_{i,s}(t) \tag{4}$$

where

- I_i is the particle's moment of inertia tensor about it's center of mass,
- $\dot{\omega}_i(t)$ is the particle's angular acceleration,
- $\tau_{i,j}(t)$ is the torque acting on particle i from particle j,
- $\tau_{i,s}(t)$ is the torque from surface forces.

The updated accelerations are then numerically integrated to get new positions and velocities. This process continues until the simulation reaches its desired final time. We direct the reader to (Davis et al., 2021) for additional information regarding the specifics of the numerical methods used in ParticLS.

The forces and torques generated between particles are calculated following a prescribed "contact law", which describes the physics of the simulated material. The surface forces acting on the particles correspond to drag loads that drive ice particle motion. The inter-particle forces, $f_{i,j}(t)$, and torques, $\tau_{i,j}(t)$, are modeled differently depending on if the particles are bonded or drifting freely. All particles are initially bonded together so we describe the cohesive contact law next.

3.1 Cohesive Contact Law

Ice floes are pieces of ice that move as a single cohesive body, whose size and shape change frequently due to fracture and re-freezing. A common approach in DEM models of sea ice is to represent each floe with an individual particle (Hopkins, 1996), (Hopkins, 2004), (Herman, 2013), (Damsgaard et al., 2018). However, this makes the floes non-deformable. (Hopkins & Thorndike, 2006) introduced representations of floes as collections of small particles bonded together that can deform via inter-particle bonds. In that work, a viscous-elastic "glue" was used to capture tensile and compressive forces between particles. (Herman, 2016) also simulated floes with multiple bonded particles, however they used disk particles, which inherently leave gaps in the floe. Similar to (Hopkins & Thorndike, 2006), we treat the initial consolidated ice pack as a collection of bonded polygons, where the evolution of floe sizes and shapes results from sequential fracture of the inter-particle bonds. The cohesive bond model approximates the behavior of an Euler-Bernoulli beam to describe the tensile, compressive, and bending forces generated between adjacent bonded particles. The equations that describe the bonded inter-particle forces and moments can be seen in (André et al., 2012). This cohesion is important for our simulations, as it has been found that stable ice arches require cohesive strength between individual ice parcels in order to sustain the stress generated in the arch (Hibler et al., 2006; Damsgaard et al., 2018). The cohesive beam model we use has not previously been applied to regional-scale simulations of sea ice, however it has been used to accurately model brittle elastic materials as collections of bonded DEM particles (André et al., 2012), (André et al., 2013), (André et al., 2017), (Nguyen et al., 2019). The beam parameters used in these simulations are summarized in Table 1.

3.2 Sea Ice Failure Model

The failure criterion for the inter-particle bonds plays a critical role in our analysis, as it dictates how the initial bonded ice pack fractures into smaller floes. We use a Mohr-Coulomb failure criterion, similar to (Weiss et al., 2007), (Rampal et al., 2016), and (Kulchitsky et al., 2017) that accounts for tensile ($\sigma_{N,t}$) and compressive ($\sigma_{N,c}$) failure thresholds:

$$\sigma_1 \leq q\sigma_2 + \sigma_c \tag{5}$$

$$\frac{\sigma_1 + \sigma_2}{2} \geq \sigma_{N,t} \tag{6}$$

$$\frac{\sigma_1 + \sigma_2}{2} \leq \sigma_{N,c} \tag{7}$$

where tension is positive, compression is negative, and σ_1 and σ_2 are the principal stresses. q and σ_c are defined following (Rampal et al., 2016; Weiss & Schulson, 2009):

$$q = \left[(\mu^2 + 1)^{1/2} + \mu\right]^2 \tag{8}$$

$$\sigma_c = \frac{2c}{(\mu^2 + 1)^{1/2} - \mu} \tag{9}$$

where μ is the internal friction coefficient, and c is the cohesion of the ice. This failure criterion has been shown to capture the mechanics of dense granular materials (Damsgaard et al., 2018), as well as the failure envelope seen in physical measurements of sea ice (Weiss et al., 2007). Similar to (Dansereau et al., 2017), we use a uniform distribution between minimum (c_{min}) and maximum (c_{max}) cohesion values when initializing our DEM particles to create heterogeneity in the ice strength and resultant failure. It is well known that bonded lattice-like DEM approaches require calibration of local parameters in order to simulate realistic macroscopic or effective response and failure properties (André et al., 2019). Therefore, we created calibration simulations to determine the appropriate local failure model values $\sigma_{N,t}$ and $\sigma_{N,c}$. We studied the uniaxial compression and tension of a 154 by 308 km block of ice composed of approximately 4000 bonded particles. The failure parameters were prescribed such that the specimen failed in tension and compression at the effective stresses found in the literature (Weiss & Schulson, 2009) for ice at geophysical scales. These failure stresses are shown in Table 1.

Failure is evaluated each time step on a per-particle basis by calculating each particle's non-local Cauchy stress tensor and then comparing it to the failure Mohr-Coulomb envelope defined above. The symmetric non-local stress tensor for a particle is defined in (Nguyen et al., 2019) as:

$$\overline{\overline{\sigma}}_{\Omega} = \frac{1}{2\Omega}\left(\sum_{j=1}^{N}\frac{1}{2}(\mathbf{r}_{i,j}\otimes\mathbf{f}_{i,j}+\mathbf{f}_{i,j}\otimes\mathbf{r}_{i,j})\right) \tag{10}$$

where

- Ω is the volume of particle i,
- N is the total number of neighboring particles,
- $\otimes$ is the tensor product between two vectors,
- $f_{i,j}$ is the force imposed on particle i from the beam between i and j,
- $r_{i,j}$ is the vector between the centroids of particles i and j.

This tensor is calculated for each particle using a neighborhood, N, comprised of all adjacent particles that the home particle is still bonded to. If the failure criteria is met, a portion of the particle's bonds are broken. This is done by finding the eigenvector of the stress tensor associated with the largest tensile principal stress and then defining a plane perpendicular to that vector. All bonds that fall on one side of this plane are then severed, as shown in Figure 6 of (André et al., 2017). Once the cohesive bonds are broken between two particles, the particles begin to interact with each other following the contact model described below. In our testing we found that local failure models were overly brittle and therefore created large amounts of fragmentation. However, the non-local approach described above seemed to limit the overly brittle nature and resulted and more stable crack paths. Although not tested here, local failure models with softening may also have a similar effect and temper the overly brittle failure.

3.3 Ridging Contact Law

Researchers have used a variety of DEM contact laws to approximate the physics of interacting pieces of ice, and many 2D contact models can approximate effects occurring in the third dimension, such as pressure ridging, which is an important mechanism for dissipating stress in the ice pack. For particles in free-drift, we adopt the elastic-viscous-plastic contact model developed in (Hopkins, 1994, 1996) to approximate the energy lost due to crushing and ridging between contacting floes. The model accounts for two regimes; one where the generated forces are small enough to maintain elastic contact, and a second where the forces are large enough that plastic deformation occurs. In both regimes, the normal force is a function of the overlap area between contacting polygons, with a viscous component related to how quickly the overlap area changes. The tangential loads are calculated with an elastic contact model that is limited by a Coulomb friction limit. See (Hopkins, 1996) for more details on this contact model. The model parameters used in these simulations are summarized in Table 1.

3.4 Atmosphere and Ocean Drag

Drag forces acting on ice due to wind and ocean currents can be described with the following quadratic laws (Hibler, 1986), (Hopkins, 2004):

$$\vec{F_a} = \rho_a C_a A_i |\vec{v_a}| \big(\vec{v_a} \cos\theta_a + \hat{k} \times \vec{v_a} \sin\theta_a\big) \tag{11}$$

$$\vec{F_o} = \rho_o C_o A_i |\vec{v_o} - \vec{v_i}| \big((\vec{v_o} - \vec{v_i}) \cos\theta_o + \hat{k} \times (\vec{v_o} - \vec{v_i}) \sin\theta_o\big) \tag{12}$$

where the $_a$, $_o$, and $_i$ subscripts correspond to quantities related to the wind, ocean, and the individual particles, respectively. The θ_a and θ_o terms are the wind and ocean turning angles, and $\hat{k}$ is a unit vector oriented in the direction normal to the sea ice plane. Often times the turning angles are assumed to be 0, which is also assumed for these simulations, thereby simplifying equations 11 and 12. It is also commonly assumed that the relative velocity between the air and ice is dominated by the wind, and therefore equation 11 only considers the wind velocity. In these 2D simulations we account for the skin drag acting on the horizontal surface of the sea ice due to the wind and ocean, and we adopt values for these coefficients that are similar to those commonly used in the literature (see Table 1) (Hopkins, 2004; Martin & Adcroft, 2010; Gladstone et al., 2001).

The DEM sea ice literature contains several ways of accounting for the torque generated by drag. Some authors ignore it altogether (see e.g., (Hopkins, 2004; Martin & Adcroft, 2010)) while others calculate the torque due to ocean drag, but not atmospheric drag (Herman, 2016). In reality, torque can result from the curl of ocean and atmosphere currents, however (Damsgaard et al., 2018) states that it is reasonable to ignore the curl of ocean and atmosphere currents on the scale of individual ice floes. Due to the length scales of our simulations we ignore the torque resulting from curl. However, we apply a resistive moment resulting from the ocean drag, similar to (Hopkins & Shen, 2001), (Sun & Shen, 2012), and (Herman, 2016), but accounting for only the drag on the submerged horizontal surface of the floe:

$$M_o = -\rho_o r^3 C_{o,h} A_{o,h} |\omega| \omega, \tag{13}$$

where r is the polygonal floe's effective moment arm, and ω is the floe's angular velocity in the z-direction. We assume the resistive moment due to wind is minimal and therefore ignore it. Due to the 2D nature of these simulations, these moments result in reduced rotation around the z-direction.

4 Particle Initialization

To initialize our particle configurations, we leverage cloud-free MODIS imagery and concepts of optimal quantization from semi-discrete optimal transport (Xin et al., 2016; Lévy & Schwindt, 2018; Bourne et al., 2018). Using Otsu's Method (Otsu, 1979) to threshold pixel intensities, we create a binary mask of sea ice in the image (see Figure 2b). We then treat this mask as a uniform probability distribution over the sea ice and find the best discrete approximation of this distribution using Lloyd's algorithm to solve the optimal quantization problem (see e.g., (Xin et al., 2016; Bourne et al., 2018)). As shown in Figure 2c, the result is a collection of points and polygonal cells over the entire domain. The polygonal cells form a power diagram, which is a generalization of a Voronoi diagram that enables cells to be weighted and thus have different sizes. Here, the cells are constructed so that they each have approximately the same overlap area with the sea ice (red region in Figure 2c). Within this framework, it is also possible to specify a distribution over cell-ice overlap area to generate particle configurations with specific floe size distributions (FSD).

The final step in our initialization process is to identify the diagram cells that fill the ice extent (Figure 2c). Clipping the diagram cells by the ice extent can create concave, triangular, or small polygons shapes, which can affect the particle dynamics. Therefore, we define our ice particle geometries with the diagram cells that fall entirely within the ice extent, and take the cells that intersect the ice extent as our boundary particles. The final result is a set of polygons matching and filling the ice extent observed in the MODIS imagery (Figure 2d).

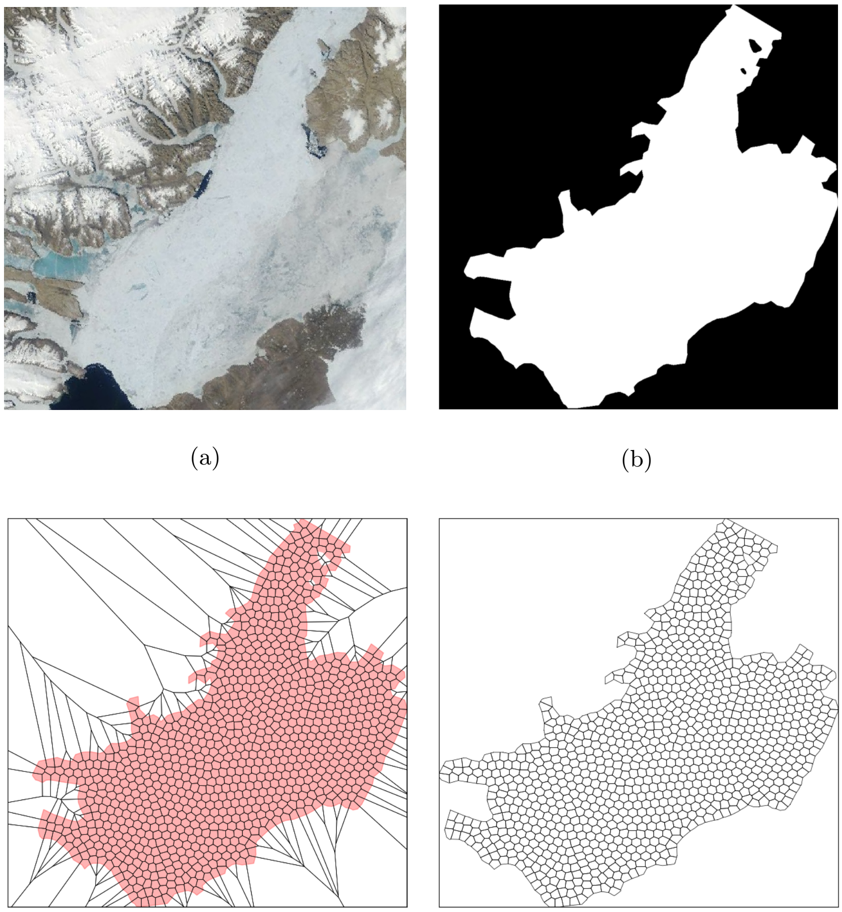

(a) (b) (c) (d)

Figure 2: Workflow for initializing polygonal ice floes from MODIS imagery. Image 2a is the MODIS imagery of the simulation domain, image 2b is a binary image reflecting ice extent used in the simulation, image 2c shows the entire set of polygons created by solving an optimal quantization problem with the ice extent outlined in red, and image 2d shows the final particle collection after clipping to the shape and extent of the input ice image. This set is intentionally a small number of particles (1000) for illustrative purposes.

5 Idealized Channel Simulation

We use a simulation domain from (Dansereau et al., 2017) as a baseline for comparing our DEM approach to continuum modeling approaches. This geometry approximates the constriction from Kane Basin into Smith Sound within Nares Strait (see dimensions in Figure 4c). Following their simulation setup, we use a stagnant ocean field and a southward wind field starting at 0 m/s and increasing linearly to $\sim$22 m/s over 24 hours, which is then held constant. This wind approximates a storm passing (Dansereau et al., 2017). The model parameters for these different simulations are presented in Table 1. The beam and ridging damping ratio parameters are multiplied by the critical damping for each type of contact model to maintain numerical stability.

The domain starts as one contiguous piece of ice spanning the entire domain. The velocity profiles in Figure 3a show how the ice initially has an hourglass-shape velocity profile along the central axis of the channel. This profile mimics the contours of the channel boundaries, and shows how the cohesive beams produce continuous velocities through the simulated ice. The principal stress profiles in Figure 3d also show a fairly continuous stress through the domain, with evidence of biaxial compression in the ice above the constricted region and biaxial tension below. The biaxial compression results from the ice being pushed into the convergent boundaries, whereas the biaxial tension results from the ice being pulled away from the divergent walls. As highlighted by (Dansereau et al., 2017), sustaining biaxial tension does not occur in standard viscous-plastic models that use elliptical failure envelopes (e.g. (Hibler III, 1979)). Using a Mohr-Coulomb failure model, like the one described in Section 3.2, allows the modeled ice to sustain the biaxial tension stresses in the lower section of the channel.

Figure 4 shows how the ice fractures from one continuous piece to many individual floes, as visualized through "beam damage", which is the number of bonds that have broken for each particle. Damage values of zero indicate particles with intact beams, whereas larger damage values indicate particles who have had several beams fail. Fracture primarily originates along the boundaries and near corners (Figure 4a), as these features create stress concentrations in the ice. The first fractures occur at the top corners of the domain, where significant tension in σ_1 (Figure 5a) results from the wind drag pulling the ice downward. Eventually the beams in these regions fail, followed by linear cracks down the vertical walls. Once these cracks form the ice in the top region is no longer held in place by the boundaries and it starts to move. This is apparent in the increase in velocity in Figure 3b for

Table 1: Model parameters used in simulations of sea ice advecting through the idealized channel and Nares Strait.

Parameter	**Symbol**	**Value**	**Units**
Ice Density	ρ_i	900.0	kg/m^3
Air Density	ρ_a	1.3	kg/m^3
Ocean Density	ρ_o	1027.0	kg/m^3
Ice Young's Modulus	E_i	5.0×10^8	Pa
Ice Poisson's Ratio	ν_i	0.3	
Ice Thickness	t_i	1.0	m
Wind Drag Coefficient	C_a	1.5×10^{-3}	
Ocean Drag Coefficient	C_o	5.5×10^{-3}	
Beam Radius Ratio	r_b	1.25e-2	
Beam Young's Modulus	E_b	5.0×10^8	Pa
Beam Poisson's Ratio	ν_b	0.3	
Beam Damping Ratio	ζ_b	0.7	
Mohr-Coulomb Internal Friction	μ	0.7	
Mohr-Coulomb Tensile Strength	$\sigma_{N,t}$	80.0×10^3	Pa
Mohr-Coulomb Compressive Strength	$\sigma_{N,c}$	-192.0×10^3	Pa
Mohr-Coulomb Minimum Cohesion	c_{min}	40×10^3	Pa
Mohr-Coulomb Maximum Cohesion	c_{max}	56×10^3	Pa
Ridging Plastic Hardening	k_{np}	928.0	Pa
Ridging Plastic Drag	k_r	26.1×10^3	N/m
Ridging Friction Coefficient	μ_r	0.3	
Ridging Damping Ratio	ζ_r	1.0	

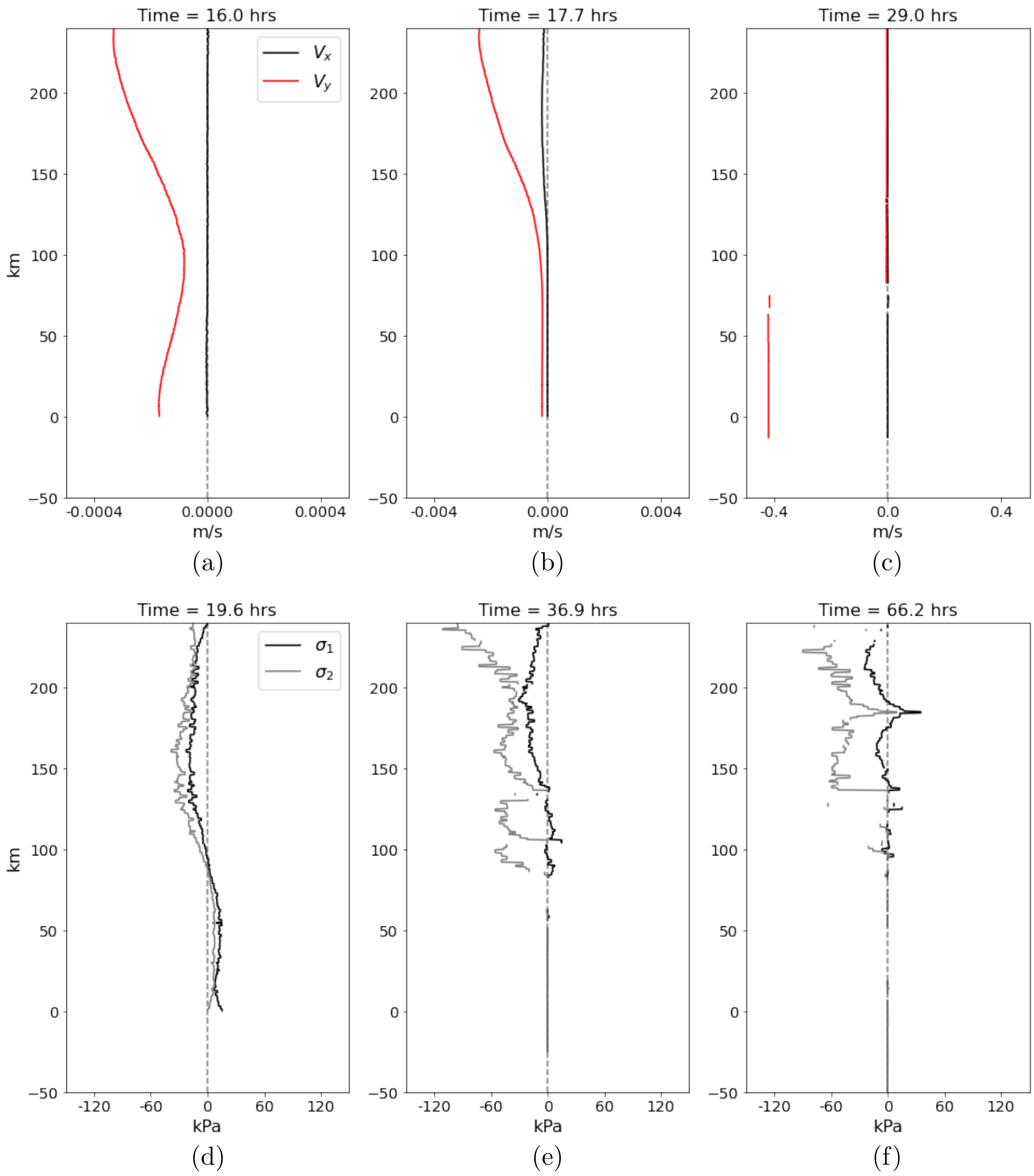

Figure 3: Velocity and principal stress profiles measured along the central axis of the idealized geometry. The y-axis corresponds to the diagram in Figure 4c, where $y = 0\,\mathrm{km}$ is the bottom of the channel geometry. Note that the velocity x-axis scale increases going from left to right.

this region of the ice. Figure 4a shows that several fractures also originate near the corners of the thinnest channel section, which correspond to regions of large tensile or shear stresses in Figure 5. A closer inspection of Figures 4a and 5a shows that these individual fractures often connect with each other to form contiguous linear cracks along the boundaries.

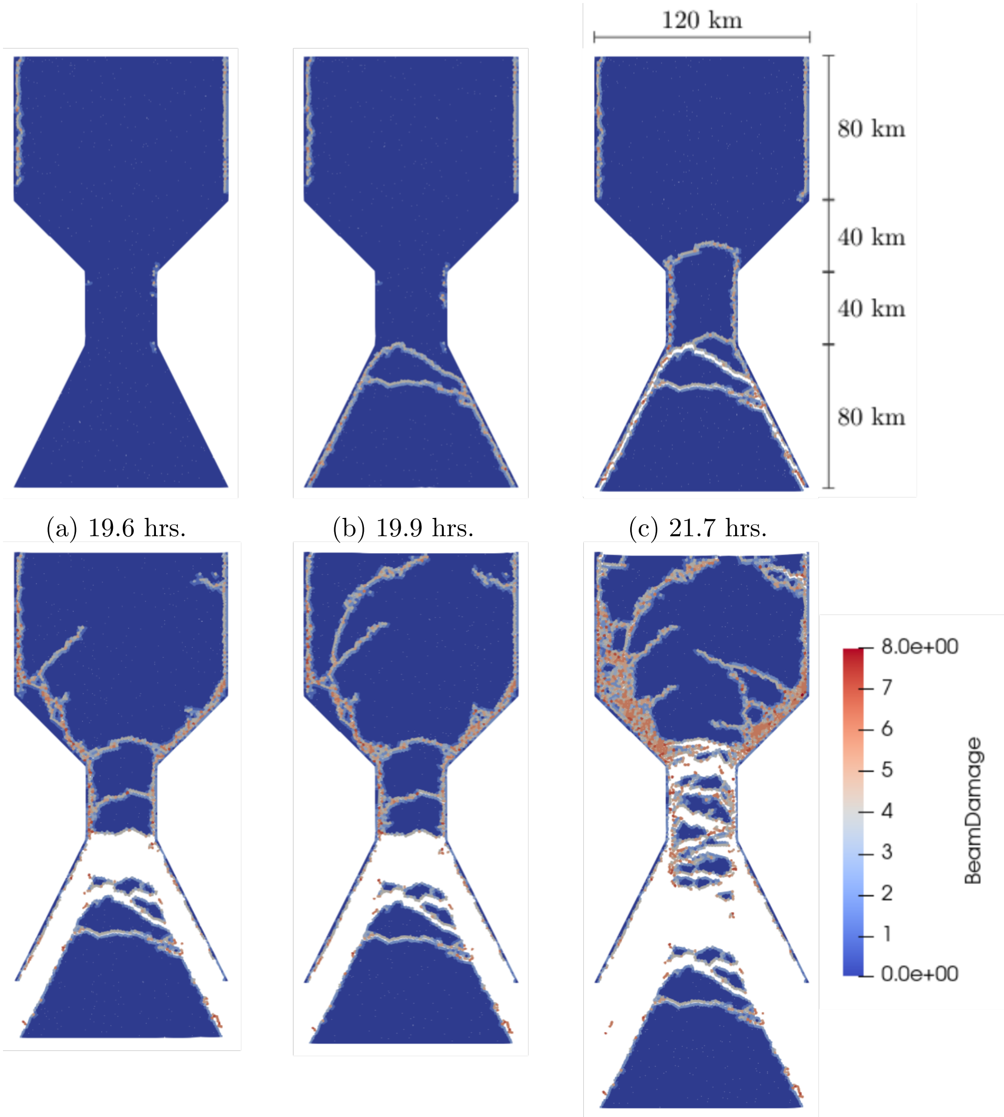

(a) 19.6 hrs. (b) 19.9 hrs. (c) 21.7 hrs.

(d) 41.3 hrs. (e) 42.8 hrs. (f) 66.4 hrs.

Figure 4: Progression of "beam damage" throughout the simulation, which reflects the number of cohesive bonds that have broken at that point in the simulation. Cracks initially form near corners along the boundaries, and then propagate into the ice pack to form arches or linear features.

The next major event in the break up sequence is the formation of two cracks along the divergent angled boundaries, which eventually connect with each other near the exit of the channel and form an arch-shaped crack (Figure 4b). At this point the ice in the lower portion of the domain is completely separated from both the boundaries and the ice above the arch, and it begins to flow south in free-drift. This is clearly seen as the discontinuity in the velocity profile (Figure 3c). This is

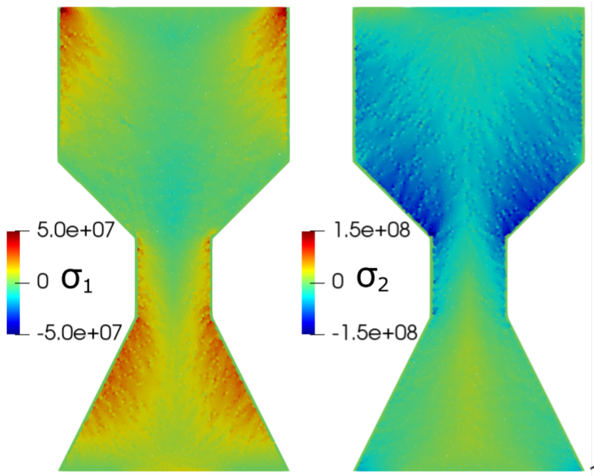

(a) 16.5 hrs.

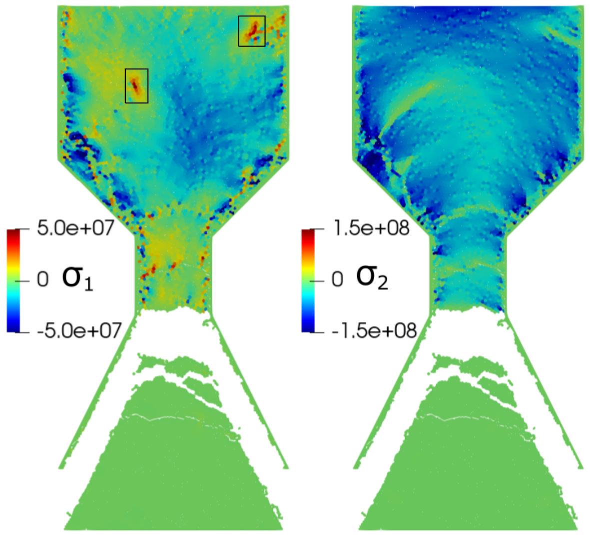

(b) 41.3 hrs.

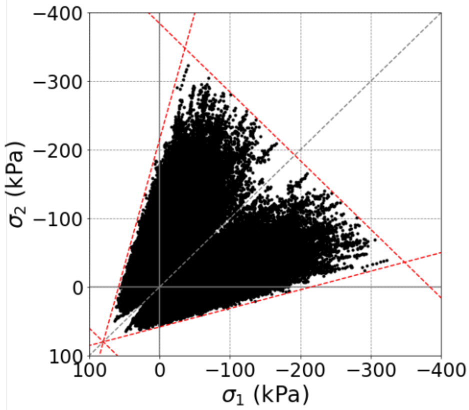

(c)

Figure 5: Images a and b show the principal stress fields before and after fracture events. Note the different scales of σ_2 between a and b, as well as the two boxes in the σ_1 b image that show the location of crack tips moving through the ice. The damage field in Figure 4d corresponds to the same time as image b. Image c shows the stress states throughout the entire simulation, where the red dashed lines indicate a Mohr-Coulomb envelope with a cohesion stress of $c = 56\,\text{kPa}$, tension failure strength of $\sigma_{N,t} = -80\,\text{kPa}$, and compression failure strength of $\sigma_{N,c} = 192\,\text{kPa}$.

an example of how the DEM is able to simulate the transition from one continuous piece of ice to multiple discrete pieces of ice. These results also show that the DEM approach is able to simulate how the arches effectively plug the constricted region and do not allow the ice above them to move - an important aspect of ice arching in nature.

After this initial arch, the stresses above the constriction become more compressive as the ice is pushed against the convergent boundaries, whereas the stresses in the ice below the arch drop to zero because the ice is in free-drift. The ice within the channel experiences large shear stresses along the boundaries (Figure 5a) and ultimately fails (Figures 4b and 4c). These fractures then connect and form a clear arch in the convergent region above the channel (Figure 4c). This is followed by several linear features emanating from the vertical and convergent boundaries that sometimes connect to form a network of cracks surrounding regions of still-bonded particles–or floes. The σ_1 image in Figure 5b shows how the cracks propagating into the ice originate from fractures along the boundaries. These crack fronts are preceded by large tensile stresses (boxed regions in Figure 5b), which means many of these leads form in tension. These biaxial tensile crack tips are also shown in the principal stress profiles; Figure 3f shows a clear biaxial tension spike at $y \sim 180\,\mathrm{km}$, which coincides with a crack reaching the central axis of the domain.

Eventually the arch at the bottom of the channel fails and the ice within the channel breaks into smaller floes, which then move south. The top arch remains fairly stable, however the ice along the convergent boundaries continues to fail as it is crushed against the walls. Although not shown, several simulations were run and the trends described here match the general progression of all results. The results from the idealized channel simulations show how the bonded DEM approach is able to capture the salient features of ice advecting through a constriction and the subsequent jamming, as well as explicit discontinuities in the ice cover. Of particular interest, Figure 5c shows the overall stress envelope of the simulated ice, and how the model is able to reconcile a continuum stress state in a DEM model where break up is explicitly captured. Next, we apply this same model to the more realistic Nares Strait geometry and estimate a distribution of floe areas and the amount of ice flowing out of Kane Basin into Smith Sound.

6 Nares Strait Simulation

In our Nares Strait simulations we once again adopt the linearly-increasing wind current and stagnant ocean current used in (Dansereau et al., 2017). The wind field is oriented down channel starting at 0 m/s and increasing to ∼22 m/s over 24 hours, which is then held constant through 72 hours. As noted by (Dansereau et al., 2017), ice motion through Nares Strait is believed to be primarily driven by winds flowing south between Ellesmere Island and Greenland. The model parameters used in these simulations are similar to those in Table 1, except for the number of particles. Our model domain is a reduced region of Nares Strait focused on Kane Basin, and we use MODIS imagery from June 28, 2003 to initialize the ice extent (see section 4 and Figure 2a). We chose the June 28, 2003 ice state because the clarity of the MODIS imagery before and after the arch fails provides a useful comparison. The resultant particle set has 8682 polygonal ice particles, and 695 stationary boundary particles. Although not shown here, we created an additional particle set with 12753 ice particles and found very similar results, suggesting that the 8682 particle set is able to capture the salient dynamics.

Figure 6 shows the break up progression in the Nares Strait simulation compared to the actual break up observed in MODIS imagery. Our model uses synthetic winds and ocean loads meaning the conditions driving the model and MODIS images in Figure 6 do not coincide. Instead, these results provide a means to qualitatively compare many of the similarities between model and observations during an arch failure event. Figure 6a shows a rounded fracture upstream of the initial arch, resulting from tensile failure near the right edge of the arch that propagates into the ice. This arch-like fracture is clearly seen as one of the first major break up events in the corresponding MODIS image. As the break up progresses to Figure 6b, additional fractures form upstream of these initial arch-like cracks, which is captured by the model (black boxes). The ice in the yellow boxes has begun to break up further, and a series linear of cracks have started emanating from the coastline as the ice is crushed and sheared against the land (green boxes).

At this point in the simulation there are multiple cracks bisecting the channel and long fractures along the boundaries that effectively separate the ice in the side inlets and channels from the ice in Kane Basin. After a period of time the cracks along the boundaries accumulate more damage as the ice is crushed against the coastline. Eventually the ice in the middle of the channel is no longer bonded to the boundaries and it begins to flow into Smith Sound. Similarly, we see that the observed ice also begins to move towards Smith Sound, but not uniformly. The ice moves fastest within a linear region extending from the exit of Kennedy Channel to the entrance to Smith Sound. The ice to the east of this region moves slower– particularly the ice near Humboldt Glacier. The model also captures the relatively stationary ice near Humboldt Glacier. The model contains multiple cracks that separate this portion of the ice from the main channel, which is predominantly landfast. The model also captures many regions of landfast ice in the fjords, inlets, and chan-

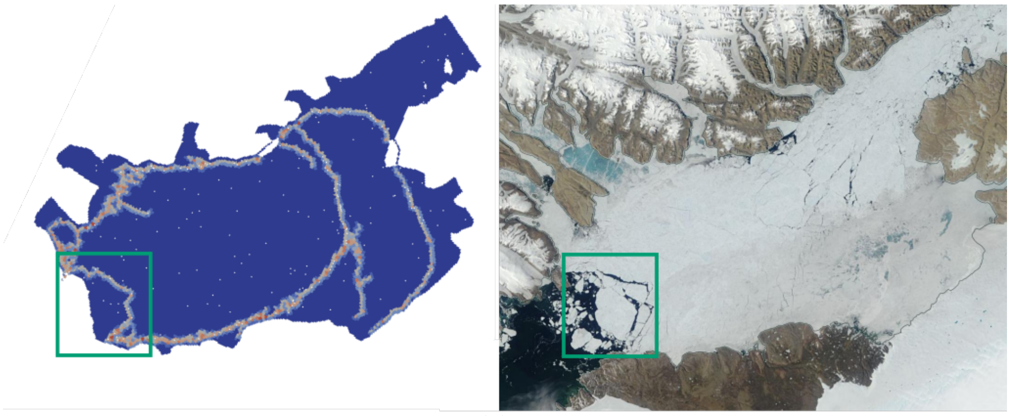

(a)

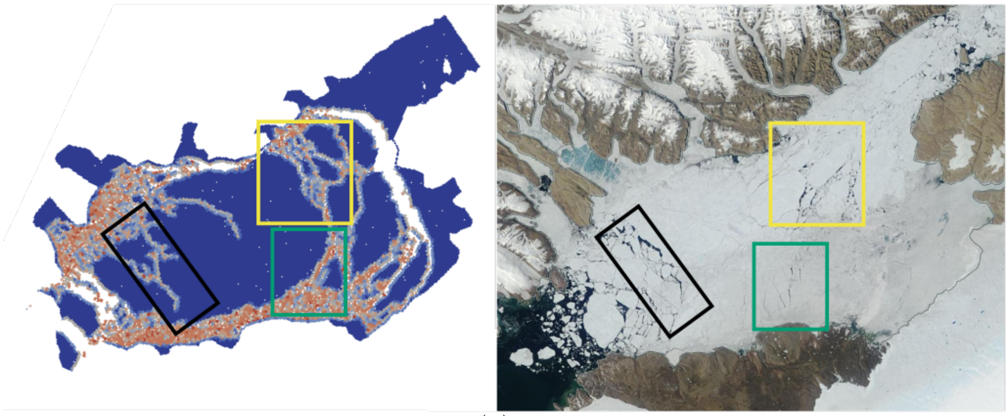

(b)

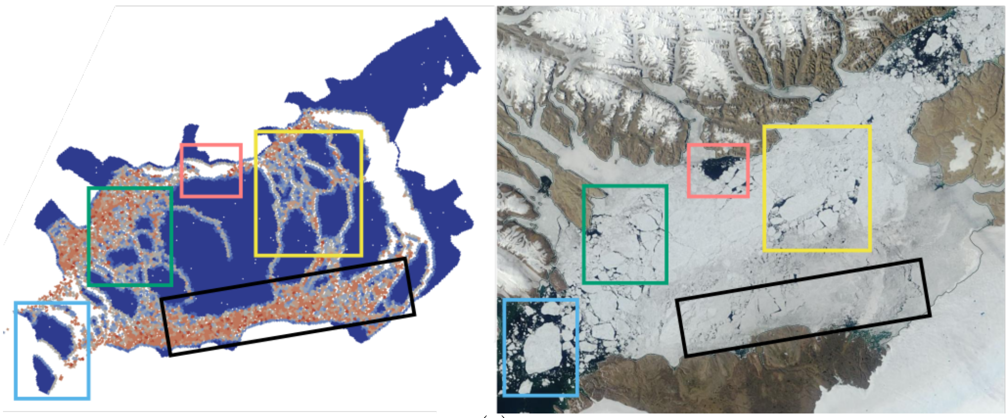

(c)

Figure 6: Comparison of "beam damage" throughout the Nares Strait simulation with MODIS images of the actual ice break up. The colored boxes indicate regions of interest where the model captures features of the real ice break up. The colorbar for the simulated results are the same as in Figure 4. The MODIS images are courtesy of NASA Earth Observing System Data and Information System (EOSDIS).

nels off of Nares Strait, which is also observed in the simulations of (Dansereau et al., 2017) and the RADARSAT observations of (Yackel et al., 2001).

The ice continues to break up as it advects out of Kane Basin (Figure 6c), and considerable break up occurs along the southern coastlines that form the constriction. The model is able to capture the ice crushing (black boxes) and breaking up into floe-like objects (green boxes) in regions similar to the MODIS imagery. Interestingly, the model also captures the formation of an open-water region (pink boxes) as the ice is sheared away from the western coastline. The ice near the exit of Kennedy channel continues to break up into many large floes (yellow boxes). One major difference between the model and observations is that the model produces a stable arch where Kennedy Channel enters Kane Basin. This arch restricts ice from advecting into the Basin, which results in the large open water region that forms near the top of the Basin. The MODIS image in Figure 6a indicates that the ice in Kennedy Channel may have had many existing flaws that are not captured in the initialized model ice. Therefore, the model likely overestimates the strength of the ice in the region, which could explain why a stable arch forms in the model, but not in the MODIS imagery. However, this arch closely matches an arch in the Nares Strait simulation of (Dansereau et al., 2017) using similar conditions (see Figure 6c 72 hour column in (Dansereau et al., 2017)). At this point the southern arch has failed completely and the ice exiting Kane Basin consists of many discrete floes. Our model produces several floe-like objects exiting the basin, which is also clearly seen in the corresponding MODIS image (light-blue boxes). (Dansereau et al., 2017) found similar floe-like behavior in their model, however one benefit of our DEM approach is its ability to model the explicit ice-ocean boundaries between these simulated floes.

Figure 7d compares distributions of floe area from three different simulations with varying cohesion values. Individual floes are identified as regions of particles that are connected to each other through cohesive beams. Images a, b, and c in Figure 7 show the floes for the three different simulations after 72 hours. Similar to (Dansereau et al., 2017), lower cohesion results in more break up, as indicated by the larger number of small floes for lower cohesion distributions in Figure 7d. Although we are unaware of any observed floe size distributions for Nares Strait in the literature, the area distributions follow the general trend of few large floes and many small floes, which match general observations from the field (Weiss & Marsan, 2004). A significant percentage of these small floes are particles whose bonds have entirely failed through crushing against the coastlines, which can be seen as the large blue

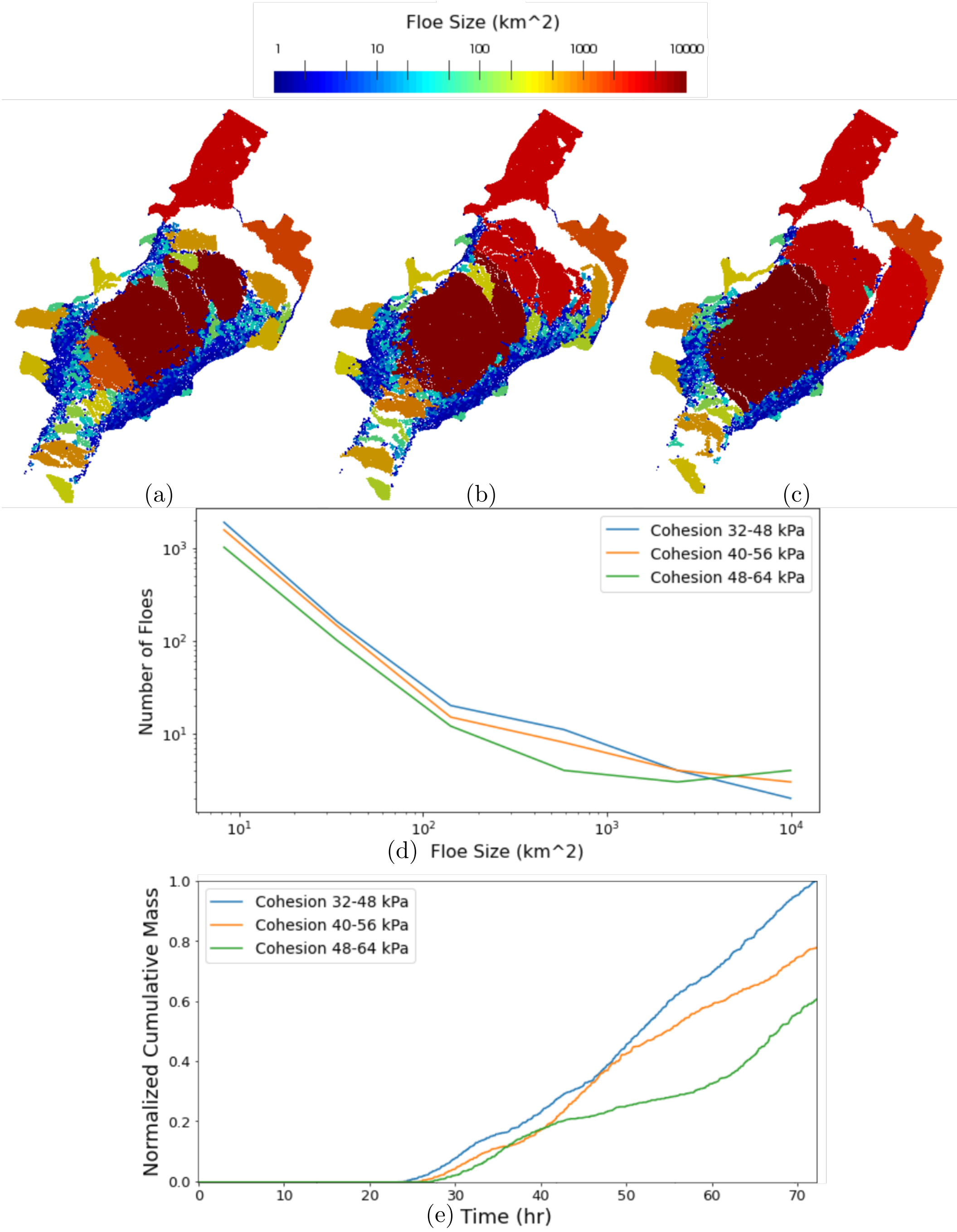

Figure 7: Floe size area (km^2) for three different simulations after 72 hours - (b) $c_{min} = 32$ kPa and $c_{max} = 48$ kPa, (c) $c_{min} = 40$ kPa and $c_{max} = 56$ kPa, (d) $c_{min} = 48$ kPa and $c_{max} = 64$ kPa. The results in b correspond to the same simulation in Figure 6. Image c is the comparison of cumulative ice mass export ice leaving Kane Basin into Smith Sound (approximately the location of the initial arch in Figure 6a).

regions in Figure 7a, b, and c. The size of these highly-damaged regions appear to increase in size as cohesion values decrease, which reflects weaker ice crushing more readily against boundaries than stronger ice.

Variation in how much the ice breaks apart directly affects the mass export out of Nares Strait. Figure 7e shows the normalized ice mass exiting Kane Basin into Smith Sound for the three simulations above. The results are normalized by the largest mass export at $T = 72$ hours for the $c_{min} = 32\,\text{kPa}$ and $c_{max} = 48\,\text{kPa}$ case in order to show general trends in the simulated ice mass export for the region. We assume a uniform ice thickness, and therefore it is difficult to compare to the simulated ice mass to observations. The ice in all three simulations start to leave Kane Basin at roughly the same time and same rate, however the final mass exports are significantly different, with lower cohesion values corresponding to larger mass export. The initial similarity in the export is related to how the initial southern arch fails. All three simulations exhibit similar southern arch failure - concentric arch-like fractures form upstream of the arch and then all ice below breaks into smaller floes. The lower cohesion ice breaks into many small floes, which are able to flow out of the basin at a higher rate than the stronger ice, which remains consolidated in larger floes. This can be seen by comparing the size of the floes that have exited Kane Basin in Figure 7a, b, and c. In addition, the secondary arches remain stable for longer periods of time with higher cohesion. This is apparent in Figure 7e where the $25 \times 10^3 - 56\,\text{kPa}$ and $30 \times 10^3 - 64\,\text{kPa}$ curves have reduced slopes for different periods of time. The initial break up corresponds to an increase in mass export, but the new arches slow the amount of ice exiting the basin. Once the secondary arches fail then we see the mass export increase again. These results indicate that weaker ice can lead to earlier outflow and more overall ice moving through Nares Strait, which supports the findings of (Dansereau et al., 2017) and (Moore et al., 2021). These results also suggest the bonded DEM could be a useful approach for studying the increase in ice export seen in recent years through Nares Strait (Moore et al., 2021), particularly as increasingly realistic ice thickness, wind forcing, and other variables are incorporated into future versions of the model.

7 Discussion and Conclusions

We present a bonded DEM method that uses a non-local Mohr-Coulomb failure model to simulate the behavior of sea ice at regional and sub-regional scales. We use an idealized channel domain and a realistic Nares Strait domain to illustrate the model's ability to capture the propagation of stress through continuous ice, and the subsequent fracture into many disparate floes. Our results capture many of the salient features of ice advecting through constricted regions and qualitatively match MODIS observations. Figures 3a, 3d, and 5a show how the model can simulate continuous velocity and stresses throughout the ice that account for boundary effects and stress concentrations. This is an important result, as it indicates we can use this DEM approach to simulate ice dynamics over large regions of contiguous ice.

Figures 3c, 3e, 3f, and 5b show how the non-local Mohr-Coulomb failure model captures realistic aspects of ice failure–namely the arch-shaped fractures that occur in ice moving through constrictions, thin linear cracks that propagate through the ice in tension, and ice crushing against solid boundaries. (André et al., 2013) showed the importance of the non-local approach in simulations of elastic brittle materials like silica glass, and our results show that this type of non-local failure model is also important for capturing realistic fracture patterns in DEM models of sea ice. Basing failure on the contributions of all particles within a localized region provides a more complete representation of the true stress state at that location within the simulated ice. The internal stress of sea ice is one of the driving factors of ice dynamics (Equation 2), and therefore we feel that considering a non-local stress in the fracture model is an important step forward towards our goal of simulating sea ice across varying spatial scales.

Comparing the Nares Strait simulation with the MODIS images in Figure 6 shows the utility of this model for simulating real world scenarios. The model is able to capture many of the salient features, including how the southern arch fractures into multiple large floes, and the development of multiple arch-like fractures upstream within Kane Basin. The model also accurately simulates landfast ice in the channels and fjords off of the Basin and near Humboldt Glacier, similar to the observations of (Yackel et al., 2001). Figure 7 shows how the modeled ice fractures into different sized floes near the exit of Kane Basin into Smith Sound, similar to the ice in Figure 6a. As expected, we see a correlation between weaker ice, earlier failure of the ice arches, and increased ice export out of the strait.

The results in Figures 4, 3, and 5 match the simulated results in (Dansereau et al., 2017) remarkably well considering the stark difference in modeling approaches. The primary difference between the two sets of results is that the DEM approach can explicitly model the leads and discontinuities post-failure. (Dansereau et al., 2017) state that their model is designed to accurately capture the dynamics of sea ice at regional ($\sim$100 km) to global ($\sim$1000 km) scales, whereas we are more interested in modeling the dynamics at regional scales and smaller, where the ice is highly discontinuous. Similarly, (Rasmussen et al., 2010) used the sea ice continuum model CICE ((Hunke et al., 2017)) coupled with an ocean model to simulate ice dynamics through Nares Strait. CICE is based on the (Hibler III, 1979) EVP rheology, but (Rasmussen et al., 2010) notes that the underlying continuum assumption begins to break down below 100 km and therefore may be unsuitable for simulating ice in Nares Strait. The proximity of the Nares Strait coastline affects the ice's stress state at much smaller scales than 100 km (Rasmussen et al., 2010). This suggests that a bonded DEM approach could supplement these continuum models for applications at sub-regional scales (<100 km) where the location of discontinuities is important. The floe area distribution in Figure 7 also illustrates how the DEM approach could serve as a useful tool for future studies investigating the evolution of floe size distributions as a function of boundary conditions, forcing functions, or material properties.

Despite the qualitative agreement between our model results, the (Dansereau et al., 2017) results, and satellite observations, there are several areas where the DEM model could be improved. First and foremost, assimilating more observational data into the model could improve accuracy. For example, we used wind speeds that approximate a large idealized storm passing through the idealized channel and Nares Strait. Actual winds were lower and more complex. As a result we see much larger displacements in that simulation than after 72 hours in the MODIS imagery. This uniform wind load and the stagnant ocean load vastly oversimplify the drag loads acting on the real ice. Incorporating more accurate wind and ocean data could improve the accuracy of the model. In addition, infusing additional data products such as SAR imagery can inform future simulations with a better understanding of the ice type (first-year or multi-year), thickness, or existing flaws, which can significantly change the ice properties. Future simulations will assimilate more data, as it's available.

At this point our model does not evolve any thermodynamics or change the ice thickness throughout the simulation. (Hibler et al., 2006) states that the Nares Strait arch may become stronger due to thermodynamic processes, which our model ignores, and could be a source of mismatch between the simulated results and observations. However, the time scales of these DEM simulations are quite short - on the order of several hours or a few days. Effects such as thermodynamic thickening likely play a smaller role in the dynamics over these short timescales. However, mechanical thickening could play an important role in these sub-regional scale simulations, particularly in the large crushing regions in Figures 6 and 7 where the ice in Nares

Strait would likely become thicker due to ridging. In fact these same regions become significantly thicker in the Nares Strait simulations in (Dansereau et al., 2017) (reference Figure 11a in (Dansereau et al., 2017)). Future DEM studies will vary the ice thickness to investigate how it affects arch stability, and how it relates to earlier arch break up and greater export out of the strait.

A known limitation with bonded DEM or lattice spring methods is the need to calibrate local model parameters (Nguyen et al., 2019). Often times setting the bond's properties such as Young's Modulus, or failure strengths to the macroscopic values of a particular material do not yield realistic results. The extra step of calibrating these parameters to achieve realistic elastic and fracture behavior can be time consuming, and does not guarantee accurate macroscopic behavior. Future work may incorporate an optimization routine to learn the appropriate model parameters from the mismatch between model output and satellite observations. Alternatively, the use of non-local distinct lattice spring (André et al., 2019), or peridynamic models (Davis et al., 2021) could avoid the need for time intensive calibration studies, and facilitate using real-world values for the model parameters.

As sea ice models continue to develop towards forecasting dynamics on tactically-relevant scales, the ability to model explicit leads and cracks in the ice may prove critical to the overall utility of the ice forecasts. These discontinuities provide potential avenues for ships to travel through, or provide obstacles for over-ice expeditions. We have shown that sea ice models based on the DEM are able to capture the complex sea ice dynamics on these scales.

Acknowledgments

This research was funded as part of the U.S. Army Program Element 060311A, Ground Advanced Technology task for Sensing and Prediction of Arctic Maritime Coastal Conditions and through the Office of Naval Research SIDEx program, grant N000142MP001. We acknowledge the use of MODIS imagery provided by the NASA Worldview application (https://worldview.earthdata.nasa.gov/), part of the NASA Earth Observing System Data and Information System (EOSDIS). Information on the ParticLS software library is included in (Davis et al., 2021), and the parameters necessary to reproduce these ParticLS simulations are described in Table 1.

References

André, D., Girardot, J., & Hubert, C. (2019). A novel dem approach for modeling brittle elastic media based on distinct lattice spring model. *Computer Methods* *in Applied Mechanics and Engineering*, *350*, 100–122.

André, D., Iordanoff, I., Charles, J.-l., & Néauport, J. (2012). Discrete element method to simulate continuous material by using the cohesive beam model. *Computer methods in applied mechanics and engineering*, *213*, 113–125.

André, D., Jebahi, M., Iordanoff, I., Charles, J.-l., & Néauport, J. (2013). Using the discrete element method to simulate brittle fracture in the indentation of a silica glass with a blunt indenter. *Computer Methods in Applied Mechanics and Engineering*, *265*, 136–147.

André, D., Levraut, B., Tessier-Doyen, N., & Huger, M. (2017). A discrete element thermo-mechanical modelling of diffuse damage induced by thermal expansion mismatch of two-phase materials. *Computer Methods in Applied Mechanics and Engineering*, *318*, 898–916.

Bourne, D. P., Schmitzer, B., & Wirth, B. (2018). Semi-discrete unbalanced optimal transport and quantization. *arXiv preprint arXiv:1808.01962*.

Damsgaard, A., Adcroft, A., & Sergienko, O. (2018). Application of discrete element methods to approximate sea ice dynamics. *Journal of Advances in Modeling Earth Systems*, *10*(9), 2228–2244.

Dansereau, V., Weiss, J., Saramito, P., & Lattes, P. (2016). A maxwell elasto-brittle rheology for sea ice modelling. *The Cryosphere*, *10*(3), 1339–1359.

Dansereau, V., Weiss, J., Saramito, P., Lattes, P., & Coche, E. (2017). Ice bridges and ridges in the maxwell-eb sea ice rheology. *The Cryosphere*, *11*(5), 2033.

Davis, A. D., West, B. A., Frisch, N. J., O'Connor, D. T., & Parno, M. D. (2021). Particls: Object-oriented software for discrete element methods and peridynamics. *Computational Particle Mechanics*, 1–13.

Dumont, D., Gratton, Y., & Arbetter, T. E. (2009). Modeling the dynamics of the north water polynya ice bridge. *Journal of Physical Oceanography*, *39*(6), 1448–1461.

Gladstone, R. M., Bigg, G. R., & Nicholls, K. W. (2001). Iceberg trajectory modeling and meltwater injection in the southern ocean. *Journal of Geophysical Research: Oceans*, *106*(C9), 19903–19915.

Herman, A. (2013). Numerical modeling of force and contact networks in fragmented sea ice. *Annals of Glaciology*, *54*(62), 114–120.

Herman, A. (2016). Discrete-element bonded-particle sea ice model design, version 1.3 a–model description and implementation. *Geoscientific Model Development*, *9*(3), 1219–1241.

Hibler, W. (1986). Ice dynamics. In *The geophysics of sea ice* (pp. 577–640). Springer.

Hibler, W., Hutchings, J., & Ip, C. (2006). Sea-ice arching and multiple flow states of arctic pack ice. *Annals of Glaciology*, *44*, 339–344.

Hibler III, W. (1979). A dynamic thermodynamic sea ice model. *Journal of physical oceanography*, *9*(4), 815–846.

Hopkins, M. A. (1994). On the ridging of intact lead ice. *Journal of Geophysical Research: Oceans*, *99*(C8), 16351–16360.

Hopkins, M. A. (1996). On the mesoscale interaction of lead ice and floes. *Journal of Geophysical Research: Oceans*, *101*(C8), 18315–18326.

Hopkins, M. A. (2004). A discrete element lagrangian sea ice model. *Engineering Computations*, *21*(2/3/4), 409–421.

Hopkins, M. A., & Hibler, W. D. (1991). Numerical simulations of a compact convergent system of ice floes. *Annals of Glaciology*, *15*, 26–30.

Hopkins, M. A., & Shen, H. H. (2001). Simulation of pancake-ice dynamics in a wave field. *Annals of Glaciology*, *33*, 355–360.

Hopkins, M. A., & Thorndike, A. S. (2006). Floe formation in arctic sea ice. *Journal of Geophysical Research: Oceans*, *111*(C11).

Hunke, E., Allard, R., Blain, P., Blockley, E., Feltham, D., Fichefet, T., ... others (2020). Should sea-ice modeling tools designed for climate research be used for short-term forecasting? *Current Climate Change reports*, 1–16.

Hunke, E., & Dukowicz, J. (1997). An elastic–viscous–plastic model for sea ice dynamics. *Journal of Physical Oceanography*, *27*(9), 1849–1867.

Hunke, E., Lipscomb, W., Jones, P., Turner, A., Jeffery, N., & Elliott, S. (2017). *Cice, the los alamos sea ice model* (Tech. Rep.). Los Alamos National Lab.(LANL), Los Alamos, NM (United States).

Jirásek, M., & Bažant, Z. P. (1995). Particle model for quasibrittle fracture and application to sea ice. *Journal of engineering mechanics*, *121*(9), 1016–1025.

Jou, O., Celigueta, M. A., Latorre, S., Arrufat, F., & Oñate, E. (2019). A bonded discrete element method for modeling ship–ice interactions in broken and unbroken sea ice fields. *Computational Particle Mechanics*, *6*(4), 739–765.

Kulchitsky, A., Hutchings, J. K., Velikhov, G., Johnson, J., & Lewis, B. (2017). *Siku sea ice discrete element method model* (Final Report No. OCS Study BOEM 2017-043). Bureau Ocean Energy Management.

Kwok, R., Toudal Pedersen, L., Gudmandsen, P., & Pang, S. (2010). Large sea ice outflow into the nares strait in 2007. *Geophysical Research Letters*, *37*(3).

Lévy, B., & Schwindt, E. L. (2018). Notions of optimal transport theory and how to implement them on a computer. *Computers & Graphics*, *72*, 135–148.

Løset, S. (1994a). Discrete element modelling of a broken ice field-part ii: simulation of ice loads on a boom. *Cold regions science and technology*, *22*(4), 349–360.

Løset, S. (1994b). Discrete element modelling of a broken ice field-part i: model development. *Cold regions science and technology*, *22*(4), 339–347.

Martin, T., & Adcroft, A. (2010). Parameterizing the fresh-water flux from land ice to ocean with interactive icebergs in a coupled climate model. *Ocean Modelling*, *34*(3-4), 111–124.

Moore, G., Howell, S., Brady, M., Xu, X., & McNeil, K. (2021). Anomalous collapses of nares strait ice arches leads to enhanced export of arctic sea ice. *Nature Communications*, *12*(1), 1–8.

Nguyen, T.-T., André, D., & Huger, M. (2019). Analytic laws for direct calibration of discrete element modeling of brittle elastic media using cohesive beam model. *Computational Particle Mechanics*, *6*(3), 393–409.

Otsu, N. (1979). A threshold selection method from gray-level histograms. *IEEE transactions on systems, man, and cybernetics*, *9*(1), 62–66.

Rallabandi, B., Zheng, Z., Winton, M., & Stone, H. A. (2017). Formation of sea ice bridges in narrow straits in response to wind and water stresses. *Journal of Geophysical Research: Oceans*, *122*(7), 5588–5610.

Rampal, P., Bouillon, S., Ólason, E., & Morlighem, M. (2016). nextsim: a new lagrangian sea ice model. *The Cryosphere*, *10*(3), 1055–1073.

Rasmussen, T. A., Kliem, N., & Kaas, E. (2010). Modelling the sea ice in the nares strait. *Ocean Modelling*, *35*(3), 161–172.

Steele, M., Zhang, J., Rothrock, D., & Stern, H. (1997). The force balance of sea ice in a numerical model of the arctic ocean. *Journal of Geophysical Research: Oceans*, *102*(C9), 21061–21079.

Sun, S., & Shen, H. H. (2012). Simulation of pancake ice load on a circular cylinder in a wave and current field. *Cold Regions Science and Technology*, *78*, 31–39.

Thorndike, A., & Colony, R. (1982). Sea ice motion in response to geostrophic winds. *Journal of Geophysical Research: Oceans*, *87*(C8), 5845–5852.

Wadhams, P. (2000). *Ice in the ocean.* CRC Press.

Weiss, J., & Marsan, D. (2004). Scale properties of sea ice deformation and fracturing. *Comptes Rendus Physique*, *5*(7), 735–751.

Weiss, J., & Schulson, E. M. (2009). Coulombic faulting from the grain scale to the geophysical scale: lessons from ice. *Journal of Physics D: Applied Physics*, *42*(21), 214017.

Weiss, J., Schulson, E. M., & Stern, H. L. (2007). Sea ice rheology from in-situ, satellite and laboratory observations: Fracture and friction. *Earth and Planetary Science Letters*, *255*(1-2), 1–8.

Xin, S.-Q., Lévy, B., Chen, Z., Chu, L., Yu, Y., Tu, C., & Wang, W. (2016). Centroidal power diagrams with capacity constraints: Computation, applications, and extension. *ACM Transactions on Graphics (TOG)*, *35*(6), 1–12.

Yackel, J., Barber, D., & Papakyriakou, T. (2001). On the estimation of spring melt in the north water polynya using radarsat-1. *Atmosphere-Ocean*, *39*(3), 195–208.